Electrochimica Acta 539 (2025) 147063

Contents lists available at ScienceDirect

Electrochimica Acta

journal homepage: www.journals.elsevier.com/electrochimica-acta

Understanding impedance spectra of a PEM fuel cell via the distribution of transport times

Andrei Kulikovsky

Forschungszentrum Jülich GmbH, Theory and Computation of Energy Materials (IET–3), Institute of Energy and Climate Research, D–52425 Jülich, Germany

ARTICLE INFO

Keywords:
Electrochemical impedance spectroscopy
Distribution of relaxation times DRT
Distribution of transport times DTT
PEM fuel cells

ABSTRACT

In PEM fuel cells, oxygen is transported through three media: the channel, the gas diffusion layer, and the cathode catalyst layer. Transport in each medium has its own characteristic frequency, so three oxygen transport peaks are expected in the distribution of relaxation times (DRT) spectrum. However, a single transport peak has typically been demonstrated in the literature. In the high-frequency range, DRT spectra of PEMFCs exhibit multiple peaks of an unknown nature. We show that these inconsistencies and phantom peaks arise due to poor description of the oxygen and proton transport processes by the Debye kernel used in the DRT. Further, it is suggested to replace the Debye kernel with the composite kernel, which better describes the oxygen and proton transport processes. The Distribution of Transport Times (DTT) transformation is illustrated using two model and one experimental impedance spectra.

1. Introduction

The unique properties of Electrochemical Impedance Spectroscopy (EIS) and advances in the electronic instrumentation have led to the widespread use of this non-invasive and operando method of PEM fuel cell characterization. This progress has been further stimulated by the development of a new technique for spectrum decoding: the Distribution of Relaxation Times (DRT) [1–6]. The apparent simplicity and availability of software for numerical DRT calculations [7] (see also [8]) has rapidly made the DRT more popular than the long-known equivalent circuit method. Today, the DRT is a "working horse" for PEMFC spectra analysis in the fuel cell community [9–16].

The DRT is an expansion of the cell impedance over an infinite series of parallel *RC*–circuit impedances [2,5]. This choice of the basis function (kernel) would have been justified if the cell impedance were largely dominated by faradaic processes. Indeed, the faradaic impedance of the cathode catalyst layer (CCL) is well described by the parallel *RC*–circuit [17].

However, a significant contribution to the cell impedance give the oxygen and proton transport, which are poorly described by the *RC*–circuit kernel. A well-known example is the Warburg finite-length (FL) impedance [17,18], which is often used to describe oxygen transport in porous layers:

$$Z_W = \frac{\tanh\sqrt{i\omega\tau}}{\sqrt{i\omega\tau}} \tag{1}$$

The Nyquist spectrum of Eq. (1) with $\tau = 1$ is shown in Fig. 1a. Fig. 1b shows the numerical DRT spectrum calculated using the imaginary part of the impedance in Fig. 1a. As can be seen, only the largest DRT peak indicates the maximum of the imaginary part, while all of the other peaks are artifacts due to poor selection of the basis function/kernel (Fig. 1b). Not surprisingly, the DRT of a real fuel cell impedance may include a number of high-frequency peaks of unknown origin [11,19,20].

Oxygen in a PEMFC is transported though the channel and further through the gas diffusion and catalyst layers. Generally, each element in this chain has its own characteristic frequency of oxygen transport, and we may expect three transport peaks in the DRT spectrum. However, upon processing of experimental spectra, typically a single peak is attributed to the oxygen transport [9,21,22]. Furthermore, the DRT of the synthetic impedance calculated from the detailed transient PEMFC performance model also did not allow to separate all of the oxygen transport peaks [10]. In addition, the proton transport in the CCL is also poorly described by the Debye kernel, which is another source of phantom high-frequency peaks in the DRT spectrum (see below).

Song and Bazant [23] and further Quattrocchi et al. [24] developed a Distribution of Diffusion Times (DDT) technique. The method is suitable for the deconvolution of the diffusion and/or the diffusion–reaction impedance of porous electrodes modeled as a system of parallel pores. However, the DDT technique is designed to characterize the reactant transport in a single porous electrode and it can hardly be applied to describe the oxygen transport through the whole PEMFC transport chain.

E-mail address: A.Kulikovsky@fz-juelich.de.

https://doi.org/10.1016/j.electacta.2025.147063
Received 24 May 2025; Received in revised form 22 July 2025; Accepted 31 July 2025
Available online 8 August 2025

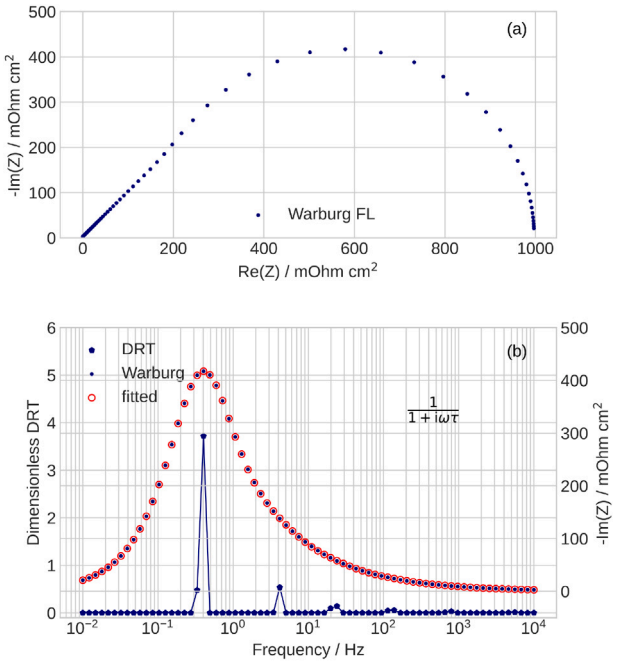

Fig. 1. (a) The Nyquist spectrum of the Warburg finite-length impedance, Eq. (1) with $\tau = 1$. (b) Solid blue line – the numerical DRT spectrum computed using the imaginary part of Z_W, solid points – $\mathrm{Im}\,(Z_W)$, open circles – $\mathrm{Im}\,(Z_W)$ reconstructed using the calculated DRT.

In this work, we separate the typical for PEMFC impedance frequency range of 0.1 Hz to 10 kHz into the low-, medium- and high-frequency domains. We construct a composite kernel, which transforms to the transport layer kernel in the LF domain, to the Debye kernel in the medium-frequency domain, and to the proton transport kernel in the HF domain. Using the two model-based synthetic impedances and an experimental impedance of a real fuel cell, we show that such a Distribution of Transport Times (DTT) allows capturing the peaks due to oxygen transport in the GDL and/or CCL, while the standard DRT misses these peaks. Furthermore, the DTT exhibits an unambiguous proton transport peak, while the DRT returns two high-frequency peaks of unknown origin.

2. Model

2.1. Impedance of a transport (gas diffusion) layer

The low-frequency part of the composite kernel for the DTT results from the problem of the oxygen transport impedance in the transport layer (TL) connected to the CCL (Fig. 2). The oxygen diffusion through the TL is described by the Fick's equation

$$\frac{\partial c_b}{\partial t} - D_b\frac{\partial^2 c_b}{\partial x^2} = 0, \quad D_b\frac{\partial c_b}{\partial x}\Big|_{x=l_t} = \frac{j_0}{4F}, \quad c_b(l_t + L) = c_h, \tag{2}$$

where x is the coordinate through the cell (Fig. 2), c_b the oxygen concentration in the TL, D_b the TL oxygen diffusivity, j_0 the current density, L the TL thickness, l_t the CCL thickness, and c_h the oxygen concentration in the channel.

To calculate the transport impedance, we need to relate the oxygen concentration and the ORR overpotential. This relation can be obtained from a simplest transient model for the catalyst layer performance. Neglecting the proton and oxygen transport losses in the catalyst layer, we write the proton charge conservation in the form

$$C_{dl}\frac{\partial \eta}{\partial t} + \frac{\partial j}{\partial x} = -i_*\left(\frac{c}{c_{ref}}\right)\exp\left(\frac{\eta}{b}\right) \tag{3}$$

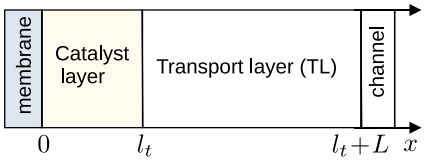

Fig. 2. Schematic of the cathode side of a PEM fuel cell. The transport layer represents the gas diffusion layer. The TL is attached to the catalyst layer with the finite (non-negligible) double layer capacitance C_{dl}.

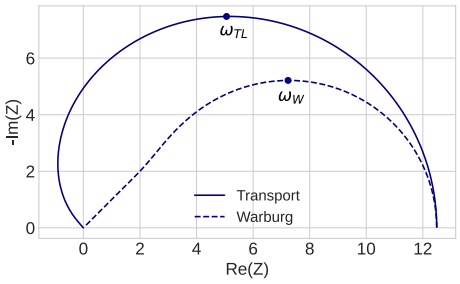

Fig. 3. The typical shapes and the characteristic frequencies of the transport and Warburg finite-length impedance.

where C_{dl} is the double layer capacitance (F cm^{-3}), η the positive by convention cathode side overpotential, j the local proton current density in the CCL, c and c_{ref} are the local and reference oxygen concentrations, i_* the ORR exchange current density, and b the ORR Tafel slope.

Due to negligible transport losses in the CCL, the overpotential is nearly independent of x and we can integrate Eq. (3) over $x \in [0, l_t]$. Setting $x = l_t$ in the resulting equation, we find

$$C_{dl}l_t\frac{\partial \eta}{\partial t} - j_0 = -i_*l_t\left(\frac{c_1}{c_{ref}}\right)\exp\left(\frac{\eta}{b}\right) \tag{4}$$

where c_1 is the oxygen concentration at the CCL/TL interface. Linearization and Fourier-transform of Eqs. (2), (4) leads to the TL impedance Z_{TL} [25,26]:

$$Z_{TL} = \left(\frac{Lj_0}{4FD_bc_{ref}}\right)\frac{\tanh\left(\sqrt{i\omega L^2/D_b}\right)}{\sqrt{i\omega L^2/D_b}\left(j_0/b + i\omega C_{dl}l_t\right)} \tag{5}$$

Eq. (5) is proportional to *the product* of the Warburg FL impedance

$$\tilde{Z}_W = \frac{\tanh\left(\sqrt{i\omega L^2/D_b}\right)}{\sqrt{i\omega L^2/D_b}} \tag{6}$$

and the parallel RC–circuit impedance representing the faradaic process in the CCL, to which the TL is attached:

$$Z_{RC} = \frac{1}{j_0/b + i\omega C_{dl}l_t}. \tag{7}$$

Thus, the TL transport impedance Z_{TL} is not equivalent to the Warburg FL impedance. Formally, reduction of Eq. (5) to the Warburg impedance corresponds to the limit of zero double layer capacitance: in this case, Z_{RC} reduces to the pure resistive term and the TL impedance, Eq. (5) transforms to the Warburg FL one. The Nyquist spectra of Z_W and Z_{TL} are illustrated in Fig. 3.

2.2. Composite kernel

Eq. (5) suggests the kernel for the transport layer impedance [27]

$$K_{TL} = \frac{\tanh\sqrt{i\omega\tau}}{\sqrt{i\omega\tau}\,(1+i\omega\tau)}, \tag{8}$$

The characteristic frequency of oxygen transport in the GDL is typically in the range of 1 to 10 Hz; it is, thus, reasonable to use Eq. (8) in expansion of the low-frequency part of the PEMFC spectrum.

The characteristic frequency of the faradaic impedance is typically belongs to the medium frequency range of 10 to 100 Hz. The faradaic impedance is well described by the Debye kernel and hence in the medium frequency range, the composite kernel should reduce to the Debye one, Eq. (9):

$$K_D(\tau,\omega) = \frac{1}{1+i\omega\tau} \tag{9}$$

The high-frequency component of the cell impedance is due to the proton transport in the CCL, which is best described by the following kernel [17,28]:

$$K_p = \frac{1}{\sqrt{i\omega\tau}\tanh\sqrt{i\omega\tau}}, \tag{10}$$

In the high-frequency domain, the composite kernel should, therefore, reduce to the proton transport kernel K_p, Eq. (10).

The proposed composite kernel K_c combines the three aforementioned kernels in one:

$$K_c(\omega,\tau) = \frac{\tanh\left(\alpha\sqrt{i\omega\tau}\right)}{\alpha\sqrt{i\omega\tau}\,(1+i\omega\tau)^{1-\beta}\left(\sqrt{i\omega\tau}\tanh\sqrt{i\omega\tau}\right)^{\beta}}, \tag{11}$$

where α and β are the step functions:

$$\alpha(\tau,\tau_\alpha) = \begin{cases} 0, & \tau \le \tau_\alpha \\ 1, & \tau > \tau_\alpha \end{cases}, \quad \beta(\tau,\tau_\beta) = \begin{cases} 1, & \tau \le \tau_\beta \\ 0, & \tau > \tau_\beta \end{cases} \tag{12}$$

with $\tau_\beta < \tau_\alpha$. At $\alpha \to 0$, we have $\tanh\left(\alpha\sqrt{i\omega\tau}\right)/(\alpha\sqrt{i\omega\tau}) \to \alpha\sqrt{i\omega\tau}/(\alpha\sqrt{i\omega\tau}) = 1$. With $\alpha = 1$ and $\beta = 0$, the kernel (11) reduces to the K_{TL} kernel, Eq. (8). With $\alpha = 0$ and $\beta = 0$, Eq. (11) transforms to the Debye kernel K_D. With $\alpha = 0$ and $\beta = 1$, Eq. (11) reduces to the proton transport kernel K_p, Eq. (10). Thus, the Debye kernel (medium-frequency) domain on the frequency scale is given by $1/(2\pi\tau_\alpha) \le f \le 1/(2\pi\tau_\beta)$. The typical low-, medium-, and high-frequency domains together with the respective K_c values are illustrated in Fig. 4.

With the composite kernel Eq. (11), the equation for the dimensionless DTT $\gamma(\tau)$ is

$$Z(\omega) = R_\infty + R_{pol}\int_{-\infty}^{\infty} K_c(\omega,\tau)\,\gamma(\tau)\,d(\ln\tau) \tag{13}$$

where R_∞ is the high-frequency (ohmic) cell resistance and R_{pol} is the polarization resistance. This equation can also be written in the form

$$\begin{aligned} Z(\omega) = R_\infty + R_{pol}\Bigg(&\int_{-\infty}^{\ln\tau_\beta} K_p(\omega,\tau)\,\gamma(\tau)\,d(\ln\tau) \\ &+ \int_{\ln\tau_\beta}^{\ln\tau_\alpha} K_D(\omega,\tau)\,\gamma(\tau)\,d(\ln\tau) \\ &+ \int_{\ln\tau_\alpha}^{\infty} K_{TL}(\omega,\tau)\,\gamma(\tau)\,d(\ln\tau)\Bigg) \end{aligned} \tag{14}$$

which explicitly shows the kernels K_p, K_D and K_{TL} for the high-, medium-, and low-frequency domains, respectively. It should be emphasized that the proposed method only requires setting the positions of the α- and β-steps on the time scale or, equivalently, on the frequency scale. This is done using an interactive plot, as discussed below.

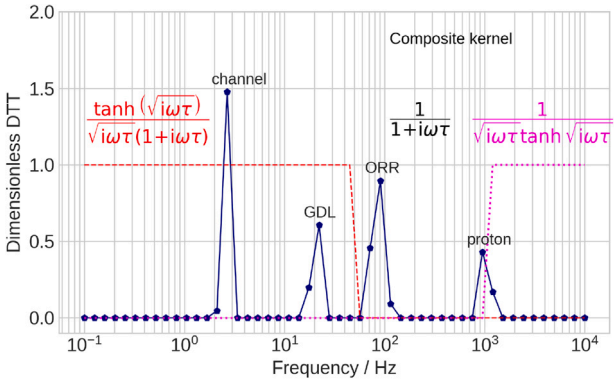

Fig. 4. The typical distribution of transport times of a PEM fuel cell and the frequency domains with the composite kernel K_c equations indicated therein. In the LF domain, K_c reduces to the transport layer kernel, Eq. (8) (red formula). In the medium frequency range, K_c reduces to the Debye kernel, Eq. (9), (black equation). In the high-frequency range, K_c is represented by the proton transport kernel K_p, Eq. (10), (magenta equation). The plots of the α– and β–functions are shown by the red dashed and dotted magenta lines, respectively.

2.3. Numerical method for DTT calculations

The numerical method originally developed to solve the standard DRT problem with the Debye kernel K_D (see Appendix in [8] and the references therein) has been modified and extended for the solution of Eq. (13) as follows. The modified method can solve the real part of Eq. (13), the imaginary part of this equation, or both the real and imaginary parts of Eq. (13) simultaneously. Depending on experimental conditions, either Z_{re}, or Z_{im} could be less noisy, and that part should be used for the DTT calculation, otherwise both the real and imaginary parts could be used.

Consider first the real part of Eq. (13)

$$\frac{Z_{re} - R_\infty}{R_{pol}} = \int_{-\infty}^{\infty} \mathrm{Re}\left(K_c(\omega,\tau)\right)\gamma(\tau)\,d(\ln\tau) \tag{15}$$

We approximate the integral in Eq. (15) on a log-scale grid

$$\delta\ln(\tau_n) = \ln(\tau_{n+1}) - \ln(\tau_n), \quad \tau_n = 1/\omega_n \tag{16}$$

using the trapezoidal rule. This results in a linear system of equations

$$\mathbf{A}\boldsymbol{\gamma} = \mathbf{b}, \quad \mathbf{b} \equiv \frac{\vec{Z}_{re} - R_\infty}{R_{pol}} \tag{17}$$

where $\boldsymbol{\gamma} = [\gamma_1,\ldots,\gamma_N]^T$, $\mathbf{b} = [b_1,\ldots,b_N]^T$, $\vec{Z}_{re} = [Z_{re,1},\ldots,Z_{re,N}]^T$ are the column vectors of the unknown function, the right side, and the real part of impedance, respectively. The matrix $\mathbf{A}$ components are given by

$$A_{m,n} = \mathrm{Re}\left(K_c(\omega_m,\tau_n)\right)\delta\ln(\tau_n). \tag{18}$$

In a Python code it is convenient to store $K_c(\omega_m,\tau_n)$ as a complex-valued matrix, e.g., K. The real part $\mathrm{Re}\left(K_c(\omega_m,\tau_n)\right)$ is computed simply by applying the operation $K[m,n]$.real.

Next, Eq. (17) is transformed into the Tikhonov regularization form

$$\left(\mathbf{A}^T\mathbf{A} + \lambda_T\mathbf{I}\right)\boldsymbol{\gamma} = \mathbf{A}^T\mathbf{b} \tag{19}$$

where $\mathbf{A}^T$ is the transposed $\mathbf{A}$, $\mathbf{I}$ is the identity matrix, and λ_T is the regularization parameter obtained by the L–curve method [29]. Eq. (19) is solved using a non-negative least-squares algorithm [30] which returns the vector $\boldsymbol{\gamma}$ satisfying to

$$\arg\min_{\boldsymbol{\gamma}}\left\{\left(\mathbf{A}^T\mathbf{A} + \lambda_T\mathbf{I}\right)\boldsymbol{\gamma} - \mathbf{A}^T\mathbf{b}\right\}, \quad \boldsymbol{\gamma} \ge 0. \tag{20}$$

Table 1
The cell operating and model parameters.

	Ref. [31]	Ref. [32]	Ref. [33]
Anode/cathode feed		H_2/air	H_2/O_2
Current density, A cm^{-2}	0.1	1.0	1.0
Cathode relative humidity		0.5	0.7
Cathode pressure, bar		1.467	1.0
Cell temperature, K		273 + 80	
Cathode flow stoichiometry		2 (air)	>10 (O_2)
CCL thickness, μm		10	8.2
GDL thickness, μm		230	150
Tafel slope, mV/exp		30	–
CCL proton conductivity, mS cm^{-1}		10	–
DL capacitance, F cm^{-3}		20	–
ORR exchange current density, A cm^{-3}		10^{-3}	–
GDL oxygen diffusivity, cm^2 s^{-1}		0.02	–
CCL oxygen diffusivity, 10^{-4} cm^2 s^{-1}	1.0	5.0	–

Here, $\boldsymbol{\gamma} \geq 0$ means that all the components of $\boldsymbol{\gamma}$ must be non-negative. Eq. (20) is solved using the *nnls* procedure from the SciPy library.

Modification of the algorithm for the imaginary part of the impedance is quite obvious: in Eq. (17) $\mathbf{b} = \vec{Z}_{im}/R_{pol}$, and in Eq. (18), $\mathrm{Re}\left(K_c(\omega_m, \tau_n)\right)$ must be replaced with $\mathrm{Im}\left(K_c(\omega_m, \tau_n)\right)$:

$$A_{m,n} = \mathrm{Im}\left(K_c(\omega_m, \tau_n)\right)\delta \ln(\tau_n). \tag{21}$$

If necessary, both the real and imaginary parts of impedance can be taken into account. In this case, the matrix $\mathbf{A}$ has $2N$ rows and N columns. The first N rows are equivalent to Eq. (18), and the last N rows are equivalent to Eq. (21). The vector $\mathbf{b}$ has the dimension $2N$ with the first N elements equal to $(\vec{Z}_{re} - R_\infty)/R_{pol}$ and the last N elements given by $\vec{Z}_{im}/R_{pol}$. Since $\mathbf{A}^T\mathbf{A}$ is the $N \times N$ matrix and the vector $\mathbf{A}^T\mathbf{b}$ is the vector with N elements, Eqs. (19), (20) do not change.

In all the examples below, the typical value of λ_T lies in the range of 10^{-4} to 10^{-3}. A delicate issue is the selection of the frequency position for the α– and β–function steps. Thanks to the fast algorithm for Eq. (20) solution, this selection can be done interactively. It is worth noting that in the code, a vanishingly small value of α is used instead of zero to avoid a zero division error.

3. Results and discussion

3.1. DTT and DRT spectra of a low-current analytical PEMFC impedance

A good test for the method proposed is comparison of the DTT and DRT spectra for the analytical impedance of a PEM fuel cell [31]. The model [31] includes oxygen transport in the channel, gas-diffusion and catalyst layers, the proton transport and faradaic reaction in the CCL. The model is constructed assuming that the cell current density is small, i.e., the variation of the static cathode overpotential through the CCL depth is small.

The Nyquist spectrum of the impedance [31] calculated for the cell current density of 100 mA cm^{-2} and the parameters in Table 1 is shown in Fig. 5a. The spectrum consists of two arcs, of which the rightmost (low frequency) one is due to the oxygen (air) transport in the cathode channel (the channel arc). The large arc represents the faradaic and proton transport in the CCL impedance, and the impedances due to the oxygen transport in the GDL and CCL. It is the task of the DTT to separate these processes.

Fig. 5b and c show the DRT and DTT spectra, respectively. The DRT spectrum consists of the four peaks, which are due to the oxygen transport in the channel (the "channel" peak), the faradaic processes (the "ORR" peak) and the proton transport (two "proton" peaks, Fig. 5b).

On the other hand, the DDT spectrum with the α and β steps at $f_\alpha \simeq 9$ Hz and $f_\beta \simeq 12$ kHz, respectively, resolves the peak due to the oxygen transport in the CCL (the "CCL" peak, Fig. 5c). The nature of the "CCL" peak in Fig. 5c has been confirmed by calculating the DTT with the twice lower CCL oxygen diffusivity $D_{ox} = 0.5 \cdot 10^{-4}$. This gave approximately twice larger area under the "CCL" peak.

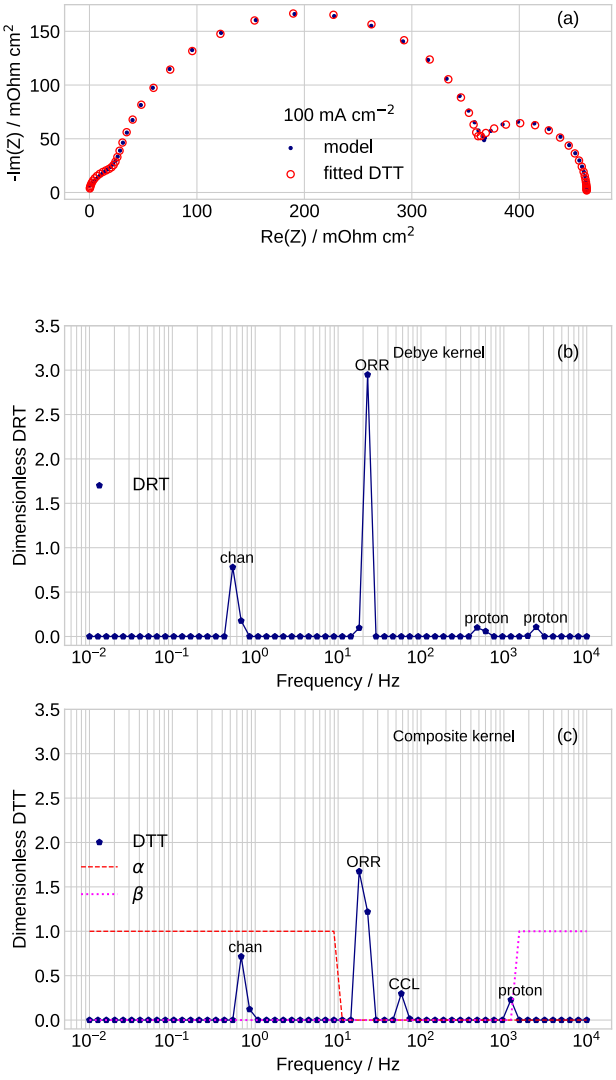

Fig. 5. (a) Blue points– the analytical Nyquist spectrum calculated using the model [31] for the cell current density of 100 mA cm^{-2} and the parameters in Table 1. Red open circles - the spectrum reconstructed (fitted) from the DTT. (b) The solid line – the classic DRT $\gamma(f)$ calculated with the imaginary part Z_{im} of impedance in (a). (c) The Distribution of Transport Times. The red dashed line – the $\alpha(f)$–function with the step frequency $f_\alpha \simeq 10$ Hz. The dotted magenta line is the β–function with the step frequency $f_\beta \simeq 1$ kHz.

A comparison of the Nyquist spectra fitted by the DRT (not shown) and DTT (Fig. 5a) shows a better quality of the DTT fitting, particularly of the channel peak. Formally, the DTT provides three times smaller residual $\|Z - Z^{fit}\|$ as compared to the DRT.

Both the DRT and DTT miss the peak due to the oxygen transport in the GDL. At low cell current density, the GDL transport impedance is small and none of the methods can detect it. Further, the DRT spectrum shows the two high-frequency peaks, which arise due to the poor description of the proton transport impedance by the Debye kernel. On the contrary, the DTT spectrum exhibits a single proton transport peak (Fig. 5c).

Table 2
A comparison of the DTT, DRT and theoretical characteristic frequencies and resistivities of the processes in the cell cathode for the spectra in Fig. 5b,c.

	Channel, O_2 transport	GDL, O_2 transport	ORR	CCL, O_2 transport	CCL, proton transport
DRT peak frequency, Hz	0.536	–	22.7	–	602, 3920
DTT peak frequency, Hz	0.677	–	18.0	57.9	1215
Theoretical frequency, Hz	0.274	15.3	26.5	46.2	855
Equation	$-\frac{3.3j_0}{8\pi F h c_{ref}\ln(1-1/\lambda)}$	$\frac{2.54D_b}{2\pi l_b^2}$	$\frac{j_0}{2\pi C_{dl} l_t b}$	$\frac{2.54D_{ox}}{2\pi l_t^2}+\frac{j_0}{8\pi F c_{ref} l_t}$	$\frac{1.71\sigma_p}{C_{dl} l_t^2}$
Reference	Ref. [34]	Ref. [18]	Ref. [17]	Ref. [35]	Ref. [28]
DRT peak resistivity, mΩ cm^2	103	–	330	–	17.3 + 12.2
DTT peak resistivity, mΩ cm^2	90.7	–	313	33.9	24.7
Theoretical resistivity, mΩ cm^2	127	12.5	300	36.2	33.3
Equation	$\frac{b}{j_0}\left(\frac{2}{(2\lambda-1)\ln(1-1/\lambda)}-\lambda\ln(1-1/\lambda)\right)$	$\frac{bl_b}{4Fc_{ref}D_b}$	$\frac{b}{j_0}$	$\frac{bl_t}{12Fc_{ref}D_{ox}}$	$\frac{l_t}{3\sigma_p}$
Reference	Ref. [36]	Ref. [37]	Ref. [17]	Ref. [37]	Ref. [17]

The position of the peak on the frequency scale gives the characteristic frequency of the process. A comparison of the DRT and DTT peak frequencies with the theoretical formulas is shown in Table 2. As can be seen, the peak frequency allows a reliable identification of the underlying process (Table 2).

The area under the peak gives the contribution of the process to the total polarization resistivity. The bottom part of Table 2 shows the resistivities calculated by integration of the peaks in Fig. 5b,c. Available in the literature equations for the partial differential resistivities and the respective numerical values are also shown in Table 2. As can be seen, the DTT peak resistivities are close to the theoretical estimates. The DTT slightly overestimates the "CCL" peak resistivity at the cost of reduced resistivity of the "channel" peak.

3.2. DRT and DTT spectra of a high-current numerical PEMFC impedance

There are no analytical models for the PEMFC impedance at a high cell current. Here, the "high current" means that the variation of the static overpotential through the CCL depth cannot be ignored. Nonetheless, the numerical model [32] can be used to generate the impedance spectrum and to compare its DTT and DRT spectra.

The cell operation regime and the oxygen transport parameters in the porous layers corresponding to 1 A cm^{-2} are shown in the second column of Table 1. The model Nyquist spectrum and the resulting DRT an DTT spectra calculated using the real part of impedance Z_{re} are shown in Fig. 6. As can be seen, the DRT misses the peak due to oxygen transport in the GDL (the "GDL" peak in Fig. 6c) and it shows a phantom peak at the frequency of about 200 Hz (Fig. 6b). This peak could erroneously be attributed to oxygen transport in the CCL.

A comparison of the characteristic frequencies and resistivities resulting from the DRT and DTT spectra is shown in Table 3. Wherever possible, theoretical estimates are also shown; however, some of the equations listed in Table 2 are not valid at high currents. Nevertheless, the data in Table 3 shows that all of the peaks in Fig. 6 could be identified using the DTT peak parameters (frequency and resistivity).

3.3. DRT and DTT spectra of an experimental impedance

For the final test, the experimental impedance spectrum of a small-scale PEM fuel cell with an active area of 0.95 cm^2 was taken [33]. The commercial MEA based on the reinforced PFSA membrane with the thickness of ≃9 μm and the ≃8.3–μm thick Pt/C cathode catalyst layer was used. The MEA was clamped between two glass fiber-reinforced PTFE gaskets with a thickness of 150 μm. The regime of the cell operation during the EIS measurements is indicated in the last column

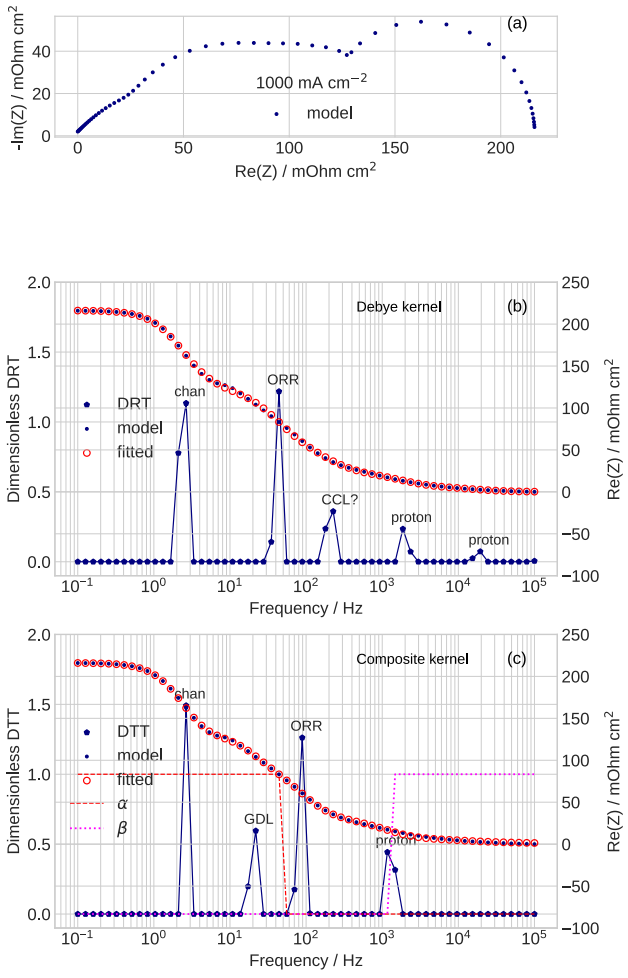

Fig. 6. (a) The Nyquist spectrum calculated using the numerical model [38] with the parameters in Table 1 for the cell current density of 1 A cm^{-3}. (b) the DRT spectrum calculated using the real part of impedance in (a). Solid points – the model Z_{re}, open circles – the reconstructed ("fitted") Z_{re} using the DRT and Eq. (13) with the Debye kernel ($\alpha=0, \beta=0$). (c) the same as in (b) for the DTT.

Table 3
A comparison of the DTT and DRT peak parameters for the spectra in Fig. 6b,c. The question mark denotes the poorly identified peak in the DRT spectrum.

	Channel, O_2 transport	GDL, O_2 transport	ORR	CCL, O_2 transport	CCL, proton transport
DRT peak frequency, Hz	2.68	–	45.0	184 (?)	1930
DTT peak frequency, Hz	2.65	21.8	88.9	–	1168
Theoretical frequency, Hz	2.74	15.3	–	–	855
DRT peak resistivity, mΩ cm^2	96.7	–	68.8	30.1 (?)	16.2
DTT peak resistivity, mΩ cm^2	75.4	40.1	72.9	–	38.4
Theoretical resistivity, mΩ cm^2	–	–	–	–	33.3

of Table 1. The spectrum has been measured with pure oxygen feed. More experimental details can be found in [33].

Before calculations, the inductive cable impedance $i\omega L_{cab}S_{cell}$ has been subtracted from the cell impedance. Here, $L_{cab} = 120$ nH is the cable inductance and S_{cell} is the cell active area. The low-frequency points with the positive imaginary part, and the high frequency points in the range of $f > 12$ kHz have been discarded.

The resulting Nyquist spectrum is shown in Fig. 7a. For the DRT and DTT calculations, the real part of the impedance was taken as it produced a much smaller residual error of the fitted spectrum than the imaginary part.

Pure oxygen feed means that the oxygen transport losses in the channel and porous layers are negligibly small and we may expect the DRT spectrum with just two peaks corresponding to the ORR and proton transport in the CCL. However, the DRT returns three peaks (Fig. 7b), of which the leftmost one is due to the ORR, and the two other peaks are due to poor description of the proton transport by the Debye kernel. On the contrary, the DTT shows two peaks (Fig. 7c), which clearly demonstrates the advantage of the composite kernel. A comparison of the DRT and DTT peak parameters is shown in Table 4. Note that the sum of the resistivities of the DRT high-frequency peaks (≃41 mΩ cm^2) is close to the resistivity of the DTT proton peak (≃36 mΩ cm^2), which confirms the nature of the high-frequency DRT peaks. Generally, the accuracy of a DRT/DTT peak resistivity is expected to depend on the residual error between the experimental and fitted impedances and on the value of the regularization parameter. To the best of our knowledge, this issue has not yet been addressed in fuel cell literature.

The regime of cell operation provides some a priori information on the number of peaks. For example, low air (oxygen) stoichiometry suggests that on the frequency scale, the leftmost peak in the DRT and DTT spectra is the "channel" one. To the right of the channel peak, a GDL peak could be expected. For typical cells, the "CCL" oxygen transport peak can be expected to the right of the large ORR peak, between the ORR and the proton transport peaks.

Useful hints for the positioning of the α and β steps on the frequency scale come from the DRT spectrum, which is displayed during the code execution. The α–step should always be located just below the main ORR peak. Our experience shows that the DTT spectrum is most sensitive to the frequency position of the β-step. This step should be positioned close to the proton transport peak, typically around 1 kHz. Fig. 8 displays a screenshot illustrating the procedure of α and β steps positioning during the code execution. Note that both the DRT and DTT spectra are displayed.

The DTT method was developed to analyze the impedance of PEM fuel cell in the current production regime. Such spectra always have finite low- and high-frequency limits, which are typically 0.1 Hz and 10 kHz, respectively. The applicability of the DTT method to other regimes and systems, is beyond the scope of this paper. Notably, the method cannot be used to analyze the impedance of a cell operating in the H_2/N_2 regime.

Finally, we emphasize that the DTT should be used alongside the DRT. The latter provides the frequency positions of the basic processes (peaks) in the system. The DTT enables us to refine this data and to search for missing peaks (Fig. 8).

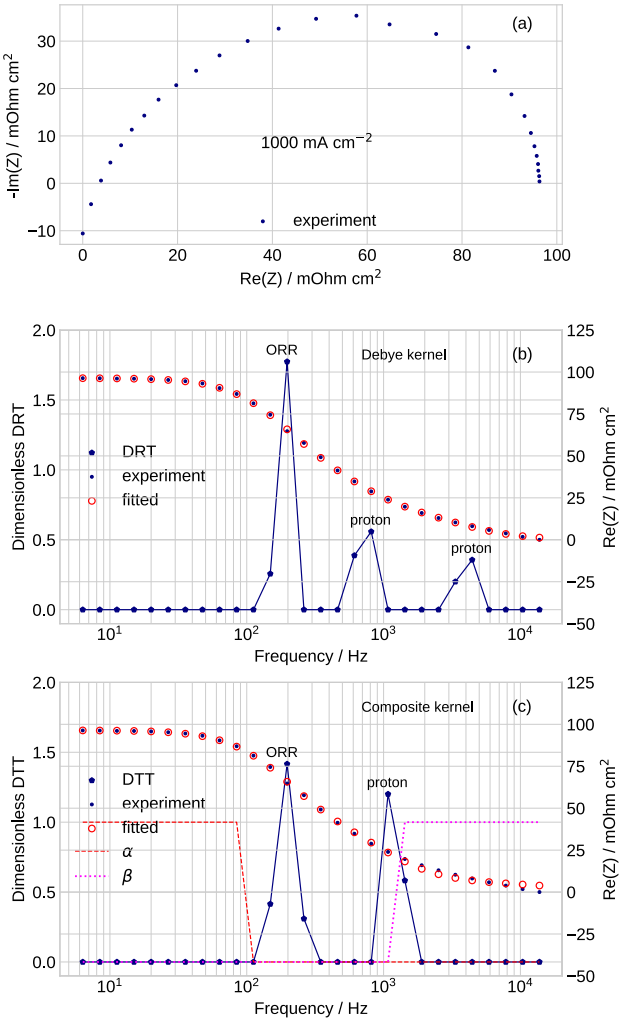

Fig. 7. (a) The experimental Nyquist spectrum of a PEM fuel cell measured at the cell current density of 1.0 A cm^{-2} [33]. (b), (c) see the caption to Fig. 6.

4. Conclusions

A composite kernel, Eq. (11), has been proposed to calculate the distribution of transport times (DTT) from a PEM fuel cell impedance. Two synthetic and one experimental impedance spectra were used to

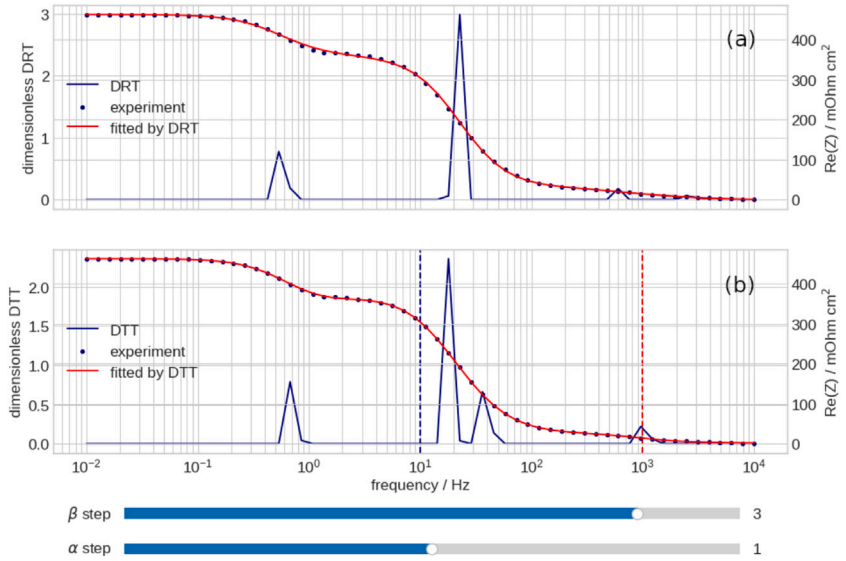

Fig. 8. The screenshot of the interactive plot displayed during code execution. (a) The static plot showing the DRT (blue solid line) calculated from the real part of the impedance (solid blue points). Red solid line – the real part fitted using the calculated DRT. (b) The dynamic plot showing the calculated DTT (blue solid line) and the real part of impedance fitted using the DTT (red solid line). The dashed lines show the position of the α–step (blue line), and β–step (red line). The sliders at the bottom allow the user to move these lines along the frequency axis using the mouse pointer. The red (fitted) line is recalculated depending on the steps positioning.

Table 4
A comparison of the DTT- and DRT-parameters for the experimental spectrum in Fig. 7a measured at the cell current density of 1.0 A cm^{-2} [33]. The regime of the cell operation is indicated in the last column of Table 1.

	ORR	CCL, proton transport
DRT peak frequency, Hz	197	812, 4440
DTT peak frequency, Hz	197	1078
DRT peak resistivity, mΩ cm^2	55.4	25.8 + 15.2
DTT peak resistivity, mΩ cm^2	58.4	48.6

calculate and compare the DTT and DRT spectra. The synthetic spectra represent the PEMFC impedance at the low air stoichiometry $\lambda = 2$, a typical value in practical applications. The experimental spectrum of a small-size PEMFC was measured by Butori et al. [33].

- A comparison of the DTT and DRT spectra calculated from the analytical low-current impedance [31], shows that the DTT resolves the peak due to the oxygen transport in the cathode catalyst layer (CCL), while the DRT misses this peak. The DRT returns two high-frequency peaks due to poor description of the proton transport in the CCL by the Debye kernel. The DTT peak frequencies enable the reliable identification of the peaks. The DTT peak resistivities agree well with the theoretical predictions.
- A comparison of the DTT and DRT spectra calculated from the numerical high-current impedance [38] shows that the DTT spectrum resolves the peak due to the oxygen transport in the GDL, which is missing in the DRT spectrum. The theoretical equations for the "channel" and "GDL" peak frequencies agree well with the respective DTT peak frequencies. However, at high cell currents, the low-current formulas for the parameters of the other peaks are not valid, so the nature of these peaks can only be guessed or verified using experimental procedures.
- The nature of the most high-frequency peak in the DRT spectrum calculated from the experimental impedance [33] is unclear. On the other hand, the DTT does not exhibit this peak, showing the advantage of the composite kernel in deciphering the high-frequency part of the cell impedance.
- It is recommended to use both the DRT and DTT for the spectra analysis.

Nomenclature

Software for the DRT and DTT calculations

The link to the most recent version of the MS Windows exe-file for the DRT and DTT calculations is available at https://github.com/akulikovsky/DTT_software

Declaration of competing interest

The authors declare that they have no known competing financial interests or personal relationships that could have appeared to influence the work reported in this paper.

Acknowledgments

The author is grateful to Dr. Martina Butori for the high-quality raw impedance spectra [33].

Data availability

Data will be made available on request.

Nomenclature

˜	Marks dimensionless variables
A	Matrix in Eq. (17)
b	ORR Tafel slope, V
b	Dimensionless right side vector, Eq. (17)
C_{dl}	Double layer volumetric capacitance, F cm^{-3}
c	Oxygen molar concentration in the CCL, mol cm^{-3}
c_b	Oxygen molar concentration in the GDL, mol cm^{-3}
c_h	Oxygen molar concentration in the channel, mol cm^{-3}
c_{ref}	Reference (inlet) oxygen concentration, mol cm^{-3}
D_b	Oxygen diffusion coefficient in the GDL, cm^2 s^{-1}
D_{ox}	Oxygen diffusion coefficient in the CCL, cm^2 s^{-1}
F	Faraday constant, C mol^{-1}
f	Frequency, Hz
f_α, f_β	Frequencies of the α- and β-steps, Hz
i_*	ORR volumetric exchange current density, A cm^{-3}
I	Unity matrix
i	Imaginary unit
j_0	Cell current density, A cm^{-2}
j	Local proton current density in the CCL, A cm^{-2}
K_c	Composite kernel, Eq. (11)
K_D	Debye kernel, Eq. (9)
K_p	Proton transport kernel, Eq. (10)
K_{TL}	Transport layer kernel, Eq. (8)
l_b	GDL thickness, cm
l_t	CCL thickness, cm
R_∞	High-frequency resistance, Ω cm^2
R_{pol}	Polarization resistance, Ω cm^2
t	Time, s
x	Coordinate through the cell, cm
Z	Impedance, Ω cm^2
Z_{RC}	Parallel RC–circuit impedance, Eq. (7), Ω cm^2
Z_{TL}	Transport layer impedance, Eq. (5), Ω cm^2
Z_W	Warburg finite-length impedance, Eq. (1), Ω cm^2
Subscripts:	
0	Membrane/CCL interface
1	CCL/GDL interface
b	In the GDL
re	Real
im	Imaginary
W	Warburg
Superscripts:	
0	Steady-state value
1	Small-amplitude perturbation
Greek:	
α, β	Step functions, Eq. (12)
γ	Dimensionless DRT and DTT functions
η	ORR overpotential, positive by convention, V
λ	Air flow stoichiometry
λ_T	Tikhonov regularization parameter
τ	Characteristic time, s
τ_α, τ_β	Characteristic time for the α– and β–steps, s
ω	Angular frequency of the AC signal, s^{-1}

References

[1] R. Fuoss, J. Kirkwood, Electrical properties of solids. viii. Dipole moments in polyvinyl chloride-diphenyl systems, J. Am. Chem. Soc. 63 (1941) 385–394, http://dx.doi.org/10.1021/ja01847a013.

[2] H. Schichlein, A.C. Müller, M. Voigts, A. Krügel, E. Ivers-Tiffée, Deconvolution of electrochemical impedance spectra for the identification of electrode reaction mechanisms in solid oxide fuel cells, J. Appl. Electrochem. 32 (2002) 875–882, http://dx.doi.org/10.1023/A:1020599525160.

[3] S. Hershkovitz, S. Tomer, S. Baltianski, Y. Tsur, ISGP: Impedance spectroscopy analysis using evolutionary programming procedure, ECS Trans. 33 (2011) 67–73, http://dx.doi.org/10.1149/1.3589186.

[4] B.A. Boukamp, Fourier transform distribution function of relaxation times; application and limitations, Electrochim. Acta 154 (2015) 35–46, http://dx.doi.org/10.1016/j.electacta.2014.12.059.

[5] E. Ivers-Tiffée, A. Weber, Evaluation of electrochemical impedance spectra by the distribution of relaxation times, J. Ceram. Soc. Jpn. 125 (2017) 193–201, http://dx.doi.org/10.2109/jcersj2.16267.

[6] F. Ciucci, Modeling electrochemical impedance spectroscopy, Curr. Opin. Electrochem. 13 (2018) 132–139, http://dx.doi.org/10.1016/j.coelec.2018.12.003.

[7] T.H. Wan, M. Saccoccio, C. Chen, F. Ciucci, Influence of the discretization methods on the distribution of relaxation times deconvolution: Implementing radial basis functions with DRTtools, Electrochim. Acta 184 (2015) 483–499, http://dx.doi.org/10.1016/j.electacta.2015.09.097.

[8] A. Kulikovsky, Impedance and resistivity of low–Pt cathode in a PEM fuel cell, J. Electrochem. Soc. 168 (2021) 044512, http://dx.doi.org/10.1149/1945-7111/abf508.

[9] Q. Wang, Z. Hu, L. Xu, Q. Gan, J. Li, X. Du, M. Ouyang, A comparative study of equivalent circuit model and distribution of relaxation times for fuel cell impedance diagnosis, Int. J. Energy Res. 45 (2021) 15948–15961, http://dx.doi.org/10.1002/er.6825.

[10] H. Yuan, H. Dai, X. Wei, P. Ming, Internal polarization process revelation of electrochemical impedance spectroscopy of proton exchange membrane fuel cell by an impedance dimension model and distribution of relaxation times, Chem. Eng. J. 418 (2021) 129358, http://dx.doi.org/10.1016/j.cej.2021.129358.

[11] G.A. Cohen, D. Gelman, Y. Tsur, Development of a typical distribution function of relaxation times model for polymer electrolyte membrane fuel cells and quantifying the resistance to proton conduction within the catalyst layer, J./Phys./Chem./C 125 (2021) 11867–11874, http://dx.doi.org/10.1021/acs.jpcc.1c03667.

[12] J.H. Kwon, P. Choi, S. Jo, H. Oh, K.-Y. Cho, Y.-K. Lee, S. Kim, K. Eom, Identification of electrode degradation by carbon corrosion in polymer electrolyte membrane fuel cells using the distribution of relaxation time analysis, Electrochim. Acta 414 (2022) 140219, http://dx.doi.org/10.1016/j.electacta.2022.140219.

[13] C. Wang, J. Li, S. Zhang, X. Li, X. Duan, Y. Wu, Q. Zhang, T. Yang, J. Liu, High-precision identification of polarization processes of proton exchange membrane fuel cells through relaxation time aanalysis: Targeted experimental design and verification, Appl. Energy 367 (2024) 123377, http://dx.doi.org/10.1016/j.apenergy.2024.123377.

[14] H. Chun, J.H. Chang, J.w. Kim, J. Sim, K. Min, Durability analysis of polymer electrolyte membrane fuel cell's gas diffusion layer based on distribution relaxation time analysis: Influence of the presence or absence of a micro-porous layer, Int. J. Hydrog. Energy 71 (2024) 831–844, http://dx.doi.org/10.1016/j.ijhydene.2024.05.154.

[15] Y. Ao, Z. Li, S. Laghrouche, D. Depernet, D. Candusso, K. Zhao, Stack-level diagnosis of proton exchange membrane fuel cell by the distribution of relaxation times analysis of electrochemical impedance spectroscopy, J. Power Sources 603 (2024) 234420, http://dx.doi.org/10.1016/j.jpowsour.2024.234420.

[16] L. Han, Y. Shang, Q. Liang, Y. Liu, Z. Guo, Distribution of relaxation times used for analyzing the electrochemical impedance spectroscopy of polymer electrolyte membrane fuel cell, Renew. Energy 227 (2024) 120485, http://dx.doi.org/10.1016/j.renene.2024.120485.

[17] A. Lasia, Electrochemical Impedance Spectroscopy and Its Applications, Springer, New York, 2014.

[18] E. Warburg, Über das Verhalten sogenannter unpolarisirbarer electroden gegen Wechselstrom, Ann. Phys. Chem. 67 (1899) 493–499, http://dx.doi.org/10.1002/andp.18993030302.

[19] A. Weiss, S. Schindler, S. Galbiati, M.A. Danzer, R. Zeis, Distribution of relaxation times analysis of high-temperature PEM fuel cell impedance spectra, Electrochim. Acta 230 (2017) 391–398, http://dx.doi.org/10.1016/j.electacta.2017.02.011.

[20] N. Bevilacqua, M. Schmid, R. Zeis, Understanding the role of the anode on the polarization losses in high-temperature polymer electrolyte membrane fuel cells using the distribution of relaxation times analysis, J. Power Sources 471 (2020) 228469, http://dx.doi.org/10.1016/j.jpowsour.2020.228469.

[21] M. Heinzmann, A. Weber, E. Ivers-Tiffée, Advanced impedance study of polymer electrolyte membrane single cells by means of distribution of relaxation times, J. Power Sources 402 (2018) 24–33, http://dx.doi.org/10.1016/j.jpowsour.2018.09.004.

[22] M. Heinzmann, A. Weber, E. Ivers-Tiffée, Impedance modelling of porous electrode structures in polymer electrolyte membrane fuel cells, J. Power Sources 444 (2019) 227279, http://dx.doi.org/10.1016/j.jpowsour.2019.227279.

[23] J. Song, M.Z. Bazant, Electrochemical impedance imaging via the distribution of diffusion times, Phys. Rev. Lett. 120 (2018) 116001, http://dx.doi.org/10.1103/PhysRevLett.120.116001.

[24] E. Quattrocchi, T.H. Wan, A. Curcio, S. Pepe, M.B. Effat, F. Ciucci, A general model for the impedance of batteries and supercapacitors: The non-linear distribution of diffusion times, Electrochim. Acta 324 (2019) 134853, http://dx.doi.org/10.1016/j.electacta.2019.134853.

[25] A. Kulikovsky, O. Shamardina, A model for PEM fuel cell impedance: Oxygen flow in the channel triggers spatial and frequency oscillations of the local impedance, J. Electrochem. Soc. 162 (2015) F1068–F1077, http://dx.doi.org/10.1149/2.0911509jes.
[26] A. Kulikovsky, Why impedance of the gas diffusion layer in a PEM fuel cell differs from the Warburg finite-length impedance? Electrochem. Comm. 84 (2017) 28–31, http://dx.doi.org/10.1016/j.elecom.2017.09.014.
[27] A. Kulikovsky, A kernel for PEM fuel cell distribution of relaxation times, Front. Energy Res. 9 (2021) 780473, http://dx.doi.org/10.3389/fenrg.2021.780473.
[28] A. Kulikovsky, Analysis of proton and electron transport impedance of a PEM fuel cell in H_2/N_2 regime, Electrochem. Sci. Adv. (2020) e202000023, http://dx.doi.org/10.1002/elsa.202000023.
[29] P.C. Hansen, Analysis of discrete ill-posed problems by means of the L-curve, SIAM Rev. 34 (1992) 561–580, http://dx.doi.org/10.2307/2132628.
[30] C.L. Lawson, R.J. Hanson, Solving Least Squares Problems, SIAM, Philadelphia, 1995.
[31] A. Kulikovsky, Analytical impedance of PEM fuel cell cathode including oxygen transport in the channel, gas diffusion and catalyst layers, J. Electrochem. Soc. 169 (2022) 034527, http://dx.doi.org/10.1149/1945-7111/ac5d97.
[32] T. Reshetenko, A. Kulikovsky, Impedance spectroscopy characterization of oxygen transport in low– and high–pt loaded PEM fuel cells, J. Electrochem. Soc. 164 (2017) F1633–F1640, http://dx.doi.org/10.1149/2.1131714jes.
[33] M. Butori, B. Eriksson, N. Nikolić, C. Lagergren, G. Lindbergh, R.W. Lindström, The effect of oxygen partial pressure and humidification in proton exchange membrane fuel cells at intermediate temperature (80–120 °C), J. Power Sources 563 (2023) 232803, http://dx.doi.org/10.1016/j.jpowsour.2023.232803.
[34] A. Kulikovsky, Analytical impedance of oxygen transport in a PEM fuel cell channel, J. Electrochem. Soc. 166 (2019) F306–F311, http://dx.doi.org/10.1149/2.0951904jes.
[35] A.A. Kulikovsky, A simple physics–based equation for low–current impedance of a PEM fuel cell cathode, Electrochim. Acta 196 (2016) 231–235, http://dx.doi.org/10.1016/j.electacta.2016.02.150.
[36] A. Kulikovsky, Analytical impedance of oxygen transport in the channel and gas diffusion layer of a PEM fuel cell, J. Electrochem. Soc. 168 (2021) 114520, http://dx.doi.org/10.1149/1945-7111/ac3a2d.
[37] A.A. Kulikovsky, One–dimensional impedance of the cathode side of a PEM fuel cell: Exact analytical solution, J. Electrochem. Soc. 162 (2015) F217–F222, http://dx.doi.org/10.1149/2.0151503jes.
[38] T. Reshetenko, A. Kulikovsky, A model for local impedance: Validation of the model for local parameters recovery from a single spectrum of PEM fuel cell, J. Electrochem. Soc. 166 (2019) F431–F439, http://dx.doi.org/10.1149/2.1241906jes.